ORIGINAL RESEARCH PAPER

A Single Layer Glucose Fuel Cell Intended as Power Supplying Coating for Medical Implants

A. Kloke[1], B. Biller[1], U. Kräling[1], S. Kerzenmacher[1]*, R. Zengerle[1,2], and F. von Stetten[1]

[1] Laboratory for MEMS Applications, Department of Microsystems Engineering – IMTEK, University of Freiburg, Georges-Koehler-Allee 106, 79110 Freiburg, Germany

[2] BIOSS Centre for Biological Signalling Studies, Albert-Ludwigs-Universität Freiburg, 79110 Freiburg, Germany

Abstract

We present a novel type of abiotically catalysed implantable glucose fuel cell with anode and cathode placed side by side, using a Raney-platinum glucose oxidation anode with high tolerance towards oxygen. In contrast to conventional assembly designs used for implantable glucose fuel cells, no permeable cathode mounted in front of the anode to effect oxygen depletion is required. At $2.2 \pm 0.1\ \mu W\ cm^{-2}$ the single layer fuel cell exhibits only half the maximum power density of the conventional fuel cell, which solely stems from the doubled total fuel cell area demand. Nevertheless, the novel single layer design is advantageous in terms of simplified fabrication and reduced overall thickness, facilitating implementation of the fuel cell as a power supplying coating directly on the surface of medical implants. Further-
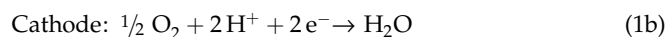
more, the single layer design offers an attractive possibility to diminish the reduction of power density by limited oxygen mass transfer to the cathode by increasing the cathode to anode area proportion. With doubled cathode area proportion a by 36% higher power density can be reached. To calculate the optimum cathode to anode area proportions, we introduced an analytical model based on the experimentally determined polarisation resistances of the individual electrodes.

Keywords: Biomedical Devices, Energy Harvesting, Implantable Glucose Fuel Cell, Oxygen Tolerant Platinum Electrodes, Power Supply

1 Introduction

1.1 Implantable Glucose Fuel Cells

Implantable glucose fuel cells represent a fully self-sufficient concept to supply low power medical implants inside the human body [1–3]. These fuel cells generate electrical energy by the separated electrochemical conversion of dissolved oxygen and glucose from body fluids. If platinum-based catalysts are used, glucose is predominantly oxidised by a two electron transfer reaction to gluconic acid [4, 5].

Anode: $Glucose + H_2O \rightarrow Gluconic\ Acid + 2\,H^+ + 2\,e^-$ (1a)

Cathode: $\frac{1}{2}\,O_2 + 2\,H^+ + 2\,e^- \rightarrow H_2O$ (1b)

Overall: $Glucose + \frac{1}{2}\,O_2 \rightarrow Gluconic\ Acid$ (1c)

As a potential option for replacement of batteries in implanted medical microdevices glucose fuel cells are superior to mechanical energy harvesting systems in terms of their continuous and accordingly more reliable power generation [1]. Such glucose fuel cells can be either catalysed by enzymes, microorganisms or abiotic catalysts [1, 6]. The use of enzymatic catalysts enabled higher power densities compared to the other concepts and has already been demonstrated in physiological environments [6–13]. For instance Cinquin et al. recently demonstrated the operation of a glucose fuel in a rat [11]. Based on a glucose oxidase anode and a polyphenol oxidase cathode this implanted fuel cell delivered $7.5\ \mu W\ mL^{-1}$ on a time scale of several hours. Nonetheless,

---

[*] Corresponding author, kerzenma@imtek.de

the lifetime of enzymatic fuel cells is strongly limited today due to enzyme denaturation typically occurring within weeks [1, 12]. The application of microorganisms in principle allows for long-term application, but their implantation bares a risk of infection [1, 14, 15].

Hence, abiotic catalyst materials are preferable over enzymes or microorganisms because of their amenability to simple heat sterilisation, low risk of infection and potential long-term stability [1]. Typically abiotic catalysts are made of noble metals or carbon but also alternative materials such as silicon nanoparticles are under current investigation [1, 16, 17]. However, despite high costs platinum catalysts are most commonly considered according to their catalytic activity and since costs in medical engineering only play a minor role.

The general tissue implantability and *in vivo* operation of such an abiotically catalysed glucose fuel cell has already been demonstrated in a dog [18], yielding a stable power density of 1.6 μW cm^{-2} over a period of 5 months. Since a cardiac pacemaker nowadays only demands 8 μW [19] and exhibits an external surface of more than 15 cm^2, it would be feasible to supply such an implant with a glucose fuel cell coated onto its external surface. If implemented as a thin layer coating onto implant surfaces such a fuel cell would not even consume additional space.

1.2 Glucose Fuel Cell Designs

When operation of a glucose fuel cell in a body tissue environment is intended, a special challenge arises: both reactants glucose and oxygen are simultaneously present in tissue fluid. On the surface of non-selective noble metal catalysts that are catalytically active towards glucose oxidation and oxygen reduction, this will result in the formation of mixed electrode potentials and consequently a drastic decrease in cell voltage and thus power output. Lacking selective abiotic catalysts for the electrooxidation of glucose in the presence of oxygen, several constructional concepts are suggested in literature to reduce the oxygen concentration at the cathode [3, 18, 20].

Figure 1A shows a stacked fuel cell design where the reactants diffuse into the fuel cell from two sides [18]. On one side

the cathode is placed behind a hydrophobic membrane, which enables only oxygen to pass through. The blockage of glucose prevents its interference during the electrochemical reduction of oxygen. A relatively thick porous noble metal anode (thickness is not further specified in Ref. [18]) for glucose oxidation is situated on the opposite side. On the surface of the noble metal anode catalyst oxygen is consumed by a direct chemical reaction with glucose. Due to the two orders of magnitude lower physiological concentration of dissolved oxygen (10^{-5} mol L^{-1}, [21]) compared to glucose (10^{-3} mol L^{-1}, [22]) this direct reaction quickly consumes all incoming oxygen. A mixed potential is thus only formed in the outmost regions of the thick anode layer. The electrode's interior is predominantly anoxic and the overall anode potential is closer to the redox potential of glucose oxidation, and hence sufficiently negative to obtain a usable cell voltage.

Rao et al. suggested a different design (*depletion design*, see Figure 1B) with an oxygen-consuming cathode mounted in front of the anode to create anoxic conditions at the anode [3, 20]. This way the extent of mixed potential formation at the anode can be reduced. The cathode is permeable to glucose and made from a glucose-insensitive catalyst for oxygen reduction (e.g. activated carbon [23]). This design has the advantage over the previously described that the reactants diffuse into the fuel cell from only one side. Therefore, the *depletion design* enables to directly mount a glucose fuel cell on top of an impermeable implant capsule.

Disadvantage of such stacked electrode assemblies is their thickness (~500 µm [24]) and the need for a lateral framework to assemble and fixate the individual layers. This renders their integration onto the implant casing cumbersome.

To facilitate the construction and integration of the fuel cell onto implant capsules we propose a novel *single layer fuel cell design*, as shown in Figure 1C. Here, anode and cathode are placed side by side on the same impermeable surface. In contrast to the previously described designs the elaborate stacking of electrode layers with a lateral framework is not required. Since no constructional workaround is applied to effect oxygen depletion at the anode, this concept requires an anode that shows sufficient tolerance towards the presence of oxygen in physiological concentrations. Otherwise mixed
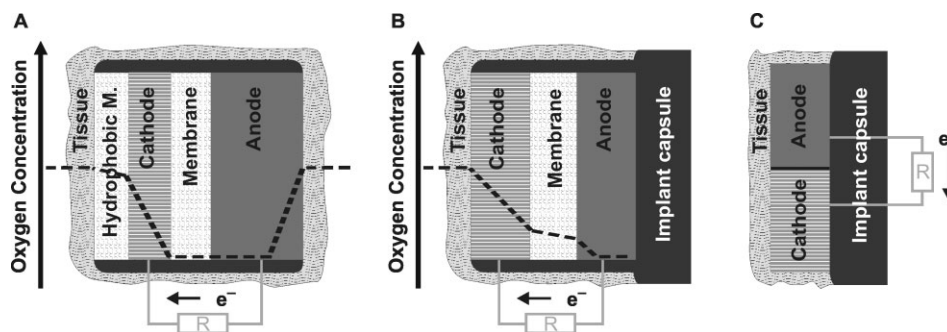

Fig. 1 Glucose fuel cell designs: (A) stacked assembly suggested by Drake et al. [18], (B) *Depletion design* proposed by Rao et al., with a selectively oxygen consuming cathode [3,20]; (C) *Single layer design* introduced in this work, electrodes are placed side by side without a lateral framework. The dashed line qualitatively indicates the progression of the oxygen concentration inside the fuel cell. In case of implantation the devices will become enclosed by a tissue capsule.

potential formation would significantly reduce cell voltage and thus power output of the fuel cell. Preliminary experiments revealed that our recently developed Raney-platinum film anodes [25] exhibit high oxygen tolerance and thus in principle fulfil this requirement.

In the present work we now quantify the oxygen tolerance of these anodes, and present correspondingly fabricated fuel cells assembled in *single layer design*. The performance of these fuel cells is compared to previously published fuel cells that were fabricated in exactly the same way, but assembled in the commonly used *depletion design* [24]. Here, silicon with KOH-etched feedholes is used as a permeable cathode substrate. Moreover, we experimentally and analytically investigate the effect of cathode to anode area proportion variation as a means to enhance the power density of single layer fuel cells.

2 Methods and Materials

2.1 Electrode Fabrication

Both electrodes are based on platinum and were fabricated using a thermal alloying process followed by chemical dissolution of the alloying partner for the creation of a highly rough catalyst surface.

Raney-platinum film anodes were prepared from 50 μm thick platinum foils (1.7×1.7 cm^2) and an electrodeposited 30 μm thick layer of zinc according to the procedure described elsewhere [25]. After annealing (48 h, 200 °C) the remaining zinc not involved in alloy formation was removed in 0.5 mol L^{-1} H$_2$SO$_4$. Subsequently, the surface of the resulting porous anode structures was cleaned by cyclic voltammetry [10 cycles, 10 mV s^{-1}, 1.3 to –0.3 V *vs*. saturated calomel reference electrode (SCE)]. To ensure comparability of the anodes their surface roughness was confirmed by analysis of the charge under the hydrogen-adsorption peaks [26]. This way an average anode roughness factor (RF, ratio of active to geometrical surface) of 2630 ± 140 was derived.

Raney-platinum film cathodes were fabricated from 500 nm of each platinum and aluminium successively evaporated onto a silicon substrate (1.7×1.7 cm^2) with 20 nm of titanium as adhesion layer [27]. Aluminium as sacrificial alloy partner was removed after annealing (1 h, 300 °C) in 1 mol L^{-1} NaOH, leaving behind a rough Pt-Al catalyst, as described in [27, 28]. Subsequent to fabrication, electrodes were cleaned and characterised by its surface roughness (RF = 175 ± 10) using cyclic voltammetry sweeps.

2.2 Characterisation of Oxygen Sensitivity of Raney-Platinum Film Anodes

After fabrication the anodes (1.7×1.7 cm^2) were cut into four equally sized pieces, each equipped with two platinum wires (50 μm thickness, ChemPur, Karlsruhe, Germany) for electrical connection, and mounted in sample holders. Each sample holder features a 2 mm thick silicone gasket that is pressed against the electrode to define the active electrode area, which in this case was 0.5×0.5 cm^2 (see reference [29] for details).

The electrode holders were placed into an aseptic electrochemical reactor with a liquid volume of 1 L as described elsewhere [29]. Subsequently the entire assembly was steam autoclaved at 121 °C for 15 min. During experiments the complete setups were held at 37 °C in an incubator.

In preliminary experiments it has been observed that oxygen concentration has a more distinct effect on the anode's open circuit potential (OCP) than on its polarisation behaviour. Therefore, the oxygen sensitivity of the anodes was investigated by recording OCPs under different oxygen and glucose concentrations in phosphate buffered saline (PBS, PBS tabs pH = 7.4, Invitrogen GmbH, Karlsruhe, Germany).

Anode OCPs were recorded against SCEs (KE11, Sensortechnik Meinsberg GmbH, Ziegra-Knobelsdorf, Germany) using the automated parallel biofuel cell testing environment described elsewhere [29]. To obtain stable equilibrium values the potentials were observed for 4,000 min. The presented values correspond to average OCP values data recorded between 3,000 and 4,000 min after the new oxygen saturation had been set. The presented standard deviations were calculated according to Gauss' law of error propagation from the deviations between the different electrodes as well as among the recorded data of each electrode.

For this investigation glucose concentrations of 0.5 and 2.5 mmol L^{-1} were chosen. These values are slightly lower than the 3.0–4.0 mmol L^{-1} reported for interstitial fluid [22] to account for the diminished glucose availability expected from tissue encapsulation.

At both glucose concentrations the OCP was investigated at oxygen saturations of 0, 3.5 and 7.0% which were set by continuously purging the testing solution with corresponding mixtures of air and nitrogen, controlled using a gas proportioner (ANALYT-MTC GmbH & Co KG, Müllheim, Germany). The applied oxygen saturations of 3.5 and 7.0% correspond to the lower and upper limits of the physiological oxygen concentration range estimated for tissue fluid [30].

Between two measurements at different oxygen concentrations the anodes were regenerated to ensure comparability between the individual experiments. This was done by cyclic voltammetry conducted under nitrogen atmosphere (10 cycles between –0.9 and 1.4 V *vs*. SCE, scan speed 10 mV s^{-1}, final value: –0.5 V *vs*. SCE).

2.3 Single Layer Fuel Cell Experiments

For fuel cell experiments the individual electrodes were contacted with two platinum wires, and mounted in sample holders as shown in Figure 2A. For cathode to anode proportions differing from the case of equally sized cathode and anode the windows in the sample holder structure defining the accessible electrode area were varied in size according to Table 1. For comparison Figure 2B shows the according setup for the previously published fuel cell realised in *depletion*
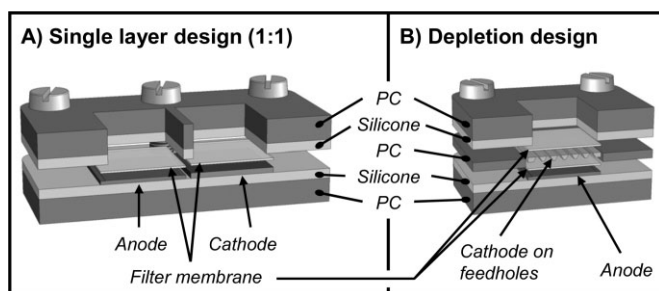
Fig. 2 Sample holder assemblies: (A) shows a sectional view of the assembly used for single layer fuel cell to realise a cathode to anode area proportion of 1:1. (B) shows the assembly of the fuel cells in *depletion design* [24]. Here silicon with KOH-etched feedholes serves as glucose permeable substrate for the cathode. Feedholes occupy 8% of the projected cathode area. Cathode and anode are separated by an additional filter membrane.

Table 1 Overview on the electrode and fuel cell areas resulting for assemblies with different cathode to anode proportions. The corresponding values for fuel cells assembled in design are given for comparison. Given are also the load steps applied to the fuel cells during the recording of polarisation curves.

		Single layer design			Depletion design
		1:1	2:1	4:1	
Cathode area	A_{Cath} (cm^{-2})	2.25	4.50	4.50	2.25
Anode area	A_{An} (cm^{-2})	2.25	2.25	1.13	2.25
Total electrode area	$A_{Cath + An}$ (cm^{-2})	4.50	6.75	5.63	4.50
Total fuel cell area	A_{FC} (cm^{-2})	4.50	6.75	5.63	2.25
Load step per fuel cell area	Δj_{FC} (µA cm^{-2})	2.2	2.2	2.1	4.4

design. As depicted in Figure 2 a Supor–450 membrane filter (0.45 µm pore size, Pall Life Sciences, East Hills, New York, USA) was placed on top of each electrode in *single layer design* and on top of the cathode in *depletion design*. This was done to experimentally simulate the diffusion resistance for glucose through a tissue capsule which is expected to form around the fuel cell device after implantation as indicated in Figure 1 [27, 31]. In *depletion design* an identical membrane filter was additionally placed between cathode and anode to guarantee electrical insulation.

As described above, the individual electrode assemblies were fixed in an aseptic electrochemical reactor, autoclaved, and subsequently the entire assembly was placed at 37 °C in an incubator. Before fuel cell experiments the electrode surfaces were cleaned electrochemically. Thereto cathodes were loaded for 1 h with an oxidative current density of 44 µA cm^{-2} in PBS (37 °C, 7% oxygen saturation, without glucose). Cleaning of the anodes was achieved by five cyclic voltammetry sweeps in PBS with 3.0 mmol L^{-1} glucose (scan range: 1.4 to –0.9 V *vs.* SCE, scan speed: 10 mV s^{-1}, final: –0.5 V *vs.* SCE, nitrogen atmosphere). Subsequently the medium was replaced by a freshly prepared saline (PBS + 3.0 mmol L^{-1} glucose).

Fuel cell experiments were performed at 7% oxygen saturation, which is the maximum oxygen concentration estimated for tissue [30], and at physiological glucose concentration (3.0 mmol L^{-1}, [22]) in PBS. To record polarisation curves a galvanostatic load was stepwise increased every 12 h during which the electrode potentials stabilised using the automated parallel biofuel cell testing environment described elsewhere [29]. According to the different fuel cell and electrode areas the current density steps had to be adjusted individually for each fuel cell assembly, as given in Table 1. Polarisation curves were constructed from the stabilised electrode potentials recorded after 12 h of operation at a given current density. Each experiment was performed with 3–4 fuel cells assembled from freshly fabricated electrodes.

3 Results and Discussion

3.1 Oxygen Sensitivity of Raney-platinum Film Anodes

As a measure for oxygen tolerance we investigated the positive shift in anode OCP resulting from an increase in oxygen concentration. Figure 3 shows the OCPs of Raney-platinum film anodes at different concentrations of oxygen (0–7.0% oxygen saturation) and glucose (0.5 and 2.5 mmol L^{-1}). For comparison also the values observed for anodes from previous works [30], fabricated from a Pt–Bi catalyst supported on hydrogel-dispersed activated carbon particles, are shown. These were obtained in a testing solution with a higher glucose concentration of 5 mmol L^{-1}.

If comparing the anode OCPs of Raney-platinum film anodes at 2.5 and 0.5 mmol L^{-1} glucose, three effects can be observed. First, the OCP in the absence of oxygen is by 74 mV more negative for the higher glucose concentration of
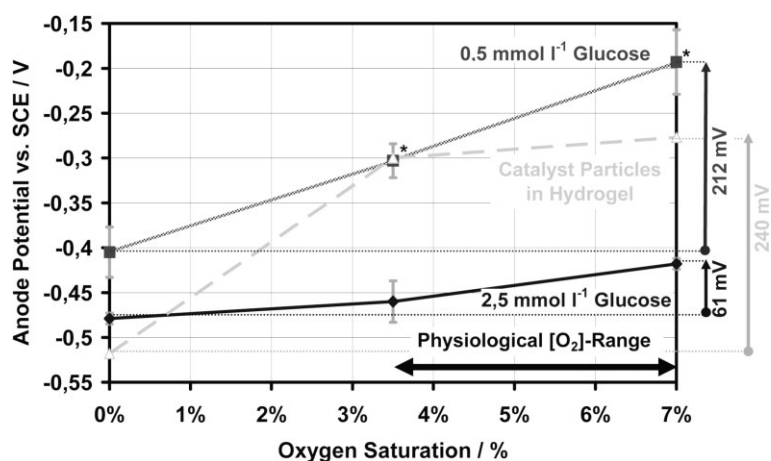

Fig. 3 Anode OCPs of the Raney-platinum film anodes at different glucose and oxygen concentrations (solid lines). For comparison data of previous anodes (extracted from Ref. [30], 5 mmol L^{-1} glucose) is provided as dashed line. The arrows on the right represent the increase in OCP for an increase in oxygen saturation from 0 to 7.0%. OCP values of Raney-platinum film anodes showing a drift instead of a stable anode potential are indicated by a star (*). Bars represent min- and max-values out of three experiments.

2.5 mmol L^{-1}. Second, the positive shift in anode OCP upon increasing oxygen saturation from 0 to 7.0% is dependent on the glucose concentration. Here, a positive shift of as much as 212 mV is observed at the lower glucose concentration of 0.5 mmol L^{-1}, while at 2.5 mmol L^{-1} glucose this shift is reduced to only 61 mV.

The observed decreasing influence of oxygen on the anode potential with increasing glucose concentration suggests an increasing oxygen depletion inside the porous anode structure (RF = 2,630 ± 140). The increased glucose concentration results in a higher reaction rate for the direct reaction between glucose (0.5 or 2.5 mmol L^{-1}) and oxygen (7% oxygen saturation, corresponding to 0.015 mmol L^{-1}) on the catalytically active electrode surface and thus to a further reduced oxygen concentration inside the pores of the electrode structure. Hence, the anode potential inside the pores is dominated by the redox potential of glucose oxidation. In a similar way platinum electrodes with high surface roughness were successfully applied to detection of glucose in the presence of lower concentrated interfering physiological substances [32, 33]. Here, an increase of surface roughness was shown to enable a dominance of glucose oxidation signal (kinetically controlled reaction) over the electrochemical response of interfering substances (diffusion-controlled reactions according to low concentration).

For comparison, the hydrogel-based anodes used in previous works exhibit an increase in anode OCP of 240 mV upon increasing the oxygen saturation from 0 to 7.0% (at 5 mmol L^{-1} glucose, [30]). This is a significantly stronger increase compared to the novel Raney-platinum film anodes. In particular, in the range of 0–3.5% oxygen saturation the hydrogel-based anodes show a significantly higher sensitivity to the presence of oxygen (positive shift of 218 mV) compared to the Raney-platinum film anodes (positive shift of 19 mV at 3 mmol L^{-1} glucose).

To evaluate the significance of oxygen sensitivity on overall fuel cell performance the increases in anode OCP due to an increase in oxygen saturation from 3.5 to 7.0% can be compared to the typical fuel cell voltage of the formerly published glucose fuel cell (698 mV, *depletion design*, [24]). According to this comparison, the 61 mV increase in anode OCP observed for Raney-platinum film anodes corresponds to a reduction in overall cell voltage of only 9%. In contrast, with the hydrogel-based anodes utilised in previous works a reduction in cell voltage of as much as 35% would be encountered.

These experiments thus demonstrated the significantly improved oxygen tolerance of Raney-platinum film anodes. The relatively small losses in anode potential to be expected upon operation of these anodes without an in front mounted oxygen consuming cathode render their application in a single layer glucose fuel cell feasible, which will be experimentally verified in the following.

3.2 Polarisation Behaviour of Single Layer Fuel Cells with Equally Sized Electrodes

Figure 4 shows electrode polarisation curves normalised to the local electrode current densities for both, glucose fuel cells implemented in the novel *single layer design* as well as glucose fuel cells assembled in state of the art *depletion design* (from previous publication [24]). The observed polarisation behaviour of cathode and anode is almost independent of fuel cell design. For both assemblies a stronger cathode than anode polarisation is observed for the linear current density range (0–8.9 µA cm^{-2}) in Table 2, indicated by their area specific resistances R_{Pol}:

$$R_{Pol} = \frac{\partial U}{\partial j} \qquad (2)$$

In both assembly designs a stronger decrease in cathode potential is observed for local current densities larger than 8.9 µA cm^{-2} which can be seen in Figure 4. This stronger decrease refers to an oxygen mass transport limitation (MTL) which has previously been observed for implantable glucose fuel cells. It originates from the low availability of oxygen under physiological conditions [24].

Moreover, no significant losses in cell voltage are observed in comparison to *depletion design* which can be ascribed to the fact that there is no in front mounted oxygen consuming cathode in *single layer fuel cells*. This has already been assumed according to the anode's oxygen tolerance derived from Figure 3. In fact, the here observed differences in cathode and anode potential between the two designs predominantly reflect fabrication caused batch to batch variations.

The observed oxygen MTL occurring at local cathode current densities above 8.9 µA cm^{-2} also dominates the polarisa-
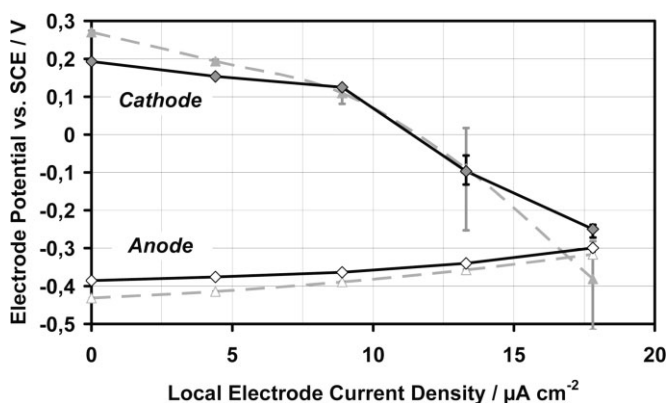

Fig. 4 Cathode and anode polarisation curves for a glucose fuel cell operated in *single layer* (solid line) and *depletion design* (dashed line) recorded in PBS + 3 mmol L^{-1} glucose at 37 °C and 7% oxygen saturation against SCE reference electrodes. Current density values are normalised by the individual electrode areas. Bars represent min- and max-values out of three experiments.

Table 2 Electrode area specific resistances R_{Pol} derived for the linear regime (0–8.9 µA cm^{-2}) of the polarisation curves shown in Figure 4.

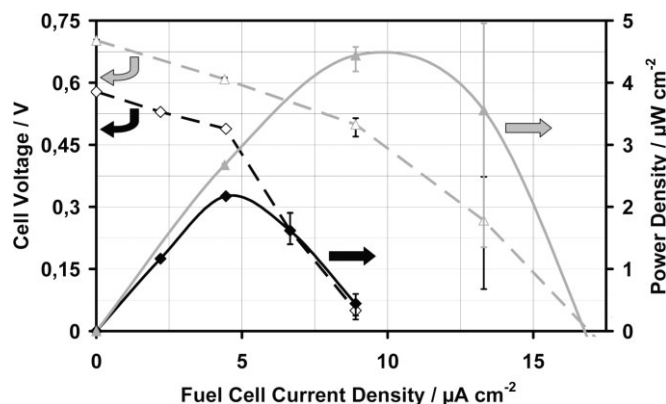|			Single layer design	Depletion design
Cathode	$R_{Pol, Cath}$	(kΩ cm^{-2})	−7.6 ± 0.3	−18.0 ± 2.4
Anode	$R_{Pol, An}$	(kΩ cm^{-2})	4.7 ± 0.7	6.5 ± 0.4
Cathode to anode polarisation ratio	$R_{Pol,Cath}/R_{Pol,An}$		1.6	2.8

Fig. 5 Cell voltage (dark and solid line) and power density (dark and dashed line) of a *single layer fuel cell* operated at 37 °C in PBS with 3.0 mmol L⁻¹ glucose and 7.0% oxygen saturation. Equivalent data for a fuel cell operated in *depletion design* is plotted in bright lines. All physical values are normalised by the fuel cells' base areas. Bars represent min- and max-values out of three experiments.

tion of the cell voltage shown in Figure 5. Because in this graph the current densities are normalised to the fuel cell's base area the cathode MTL occurs at two times lower fuel cell current densities j_{FC} in case of *single layer design* compared to in *depletion design*.

This effect originates from the 50% lower cathode area A_{Cath} in the case of *single layer fuel cells* (see Table 1). Therefore, also the corresponding fuel cell current density ($j_{FC,lim}$) at which MTL occurs at the cathode is two times lower according to:

$$j_{FC} = j_{Cath} \frac{A_{Cath}}{A_{FC}} \qquad (3)$$

This means that at the same fuel cell current density j_{FC} cathode and anode in *single layer design* face twice the current load compared to *depletion design*.

In accordance with the 50% lower total electrode area, *single layer fuel cells* also exhibit only half the maximum power density of fuel cells assembled in *depletion design* (2.2 ± 0.1 μW cm⁻² compared to 4.4 ± 0.2 μW cm⁻², see Figure 5). Nevertheless, the observed power density of 2.2 ± 0.1 μW cm⁻² clearly confirms the general feasibility of the *single layer design*. Furthermore, the results show that with Raney-platinum film anodes the use of an oxygen consuming cathode mounted in front of the anode has no significant effect on the anode potential and thus overall fuel cell power density.

In the previous experiments, the occurrence of oxygen MTL at the cathode turned out to be the key limiting factor which determines the maximum power density. Furthermore, in both designs the cathode shows a significantly stronger polarisation than the anodes. To counteract these two effects we in the following enlarge the cathode to anode area proportion ϕ:

$$\Phi = \frac{A_{Cath}}{A_{An}} \qquad (4)$$

The utilisation of an enlarged cathode to anode area proportion will allow distributing the applied fuel cell current density over an accordingly larger cathode area. This leads to a lower local cathode current density as can be derived from Eq. (5):

$$j_{Cath} = j_{FC} \frac{A_{FC}}{A_{Cath}} = j_{FC} \frac{(\Phi + 1)}{\Phi} \qquad (5)$$

Because the occurrence of MTLs is dependent on the local cathode current density j_{Cath}, an enlarged cathode proportion allows for higher overall fuel cell current densities j_{FC} without the influence of MTL at the cathode. Hence, higher cathode proportions promise to enhance the power density of *single layer fuel cells*.

Given that the fuel cell current density j_{FC} is the same, an enlarged cathode area proportion also leads to an accordingly higher local anode current density j_{An}:

$$j_{An} = j_{FC} \frac{A_{FC}}{A_{An}} = j_{FC} (\Phi + 1) \qquad (6)$$

In the following we experimentally verify the predicted consequences of enlarged cathode area proportions. Subsequently, we use an analytical model to derive maximum power densities achievable with *single layer fuel cells* as a function of their cathode area proportion ϕ.

3.3.1 Performance of Single Layer Fuel Cells at Different Cathode to Anode Area Proportions

Figure 6 shows the individual cathode polarisation curves of *single layer fuel cells* with cathode area proportions of $\phi = 1$, 2 and 4, normalised to the fuel cell current density. For comparison, also the polarisation curve of a cathode in *depletion design* is given. For *single layer fuel cells* with $\phi = 2$ the occurrence of an accelerated decrease of cathode potential, indicating an MTL, is observed at fuel cell current densities above 6.7 μA cm⁻². This means that the linear current density regime is enlarged by ~50% compared to equally sized electrodes ($\phi = 1$), where a linear polarisation behaviour is only
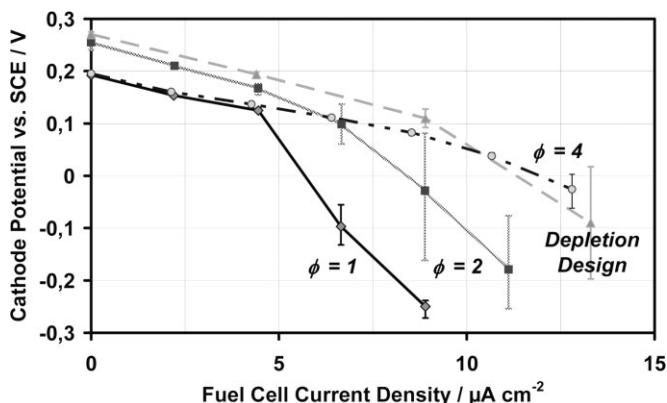

Fig. 6 Cathode polarisation curves for *single layer fuel cells* with various cathode to anode area proportions normalised to the fuel cell's base area. A cathode operated in *depletion design* is shown for comparison. Bars represent min- and max-values out of three experiments.

observed for fuel cell current densities of up to 4.5 μA cm^{-2}. For a cathode to anode area proportion of $\phi = 4$, the linear range is even enlarged to a fuel cell current density of 8.5 μA cm^{-2}. These results are in good agreement with the prediction that enlarged cathode area proportions lead to an extended linear fuel cell current density range, as derived from Eq. (5).

The second prediction derived from Eq. (5) was that enlarged cathode area proportions would lead to reduced cathode polarisation slopes. However, this prediction cannot be observed from the experimental results shown in Figure 6 due to a considerable batch-to-batch variation in cathode performance. An average area specific resistance $R_{Pol,Cath}$ of -11.8 ± 3.9 kΩ cm^{-2} (coefficient of variation of 33%) is observed for all cathodes tested in *single layer design*.

Figure 7 shows corresponding anode polarisation curves of *single layer fuel cells* with cathode to anode area proportions of $\phi = 1$, 2 and 4. In case of a cathode to anode area proportion of $\phi = 4$ a significantly stronger anode polarisation slope is obtained as compared to equally sized electrodes. Moreover, a non-linear polarisation behaviour is observed indicating that in the case of $\phi = 4$ the anode becomes subject to MTL.

As for the cathodes, the expected increase in anode polarisation slope due to the use of enlarged cathode area proportions is not clearly observable from the polarisation curves (Figure 7). Significant batch to batch variations are observed for the average area specific resistance among all anodes tested in *single layer design* (3.7 $\pm$ 1.0 kΩ cm^{-2}, coefficient of variation of 27%).

Figure 8 shows the resulting power densities obtained for *single layer fuel cells* with different cathode to anode proportions. Compared to the case of equally sized electrodes a cathode to anode area proportion of $\phi = 2$ leads to a by 36% increased power density of 3.0 $\pm$ 0.3 μW cm^{-2}. This results from the enlarged cathode area shifting the occurrence of MTL to fuel cell current densities higher than 6.7 μA cm^{-2}, as compared to higher than 4.3 μA cm^{-2} with equally sized electrodes.
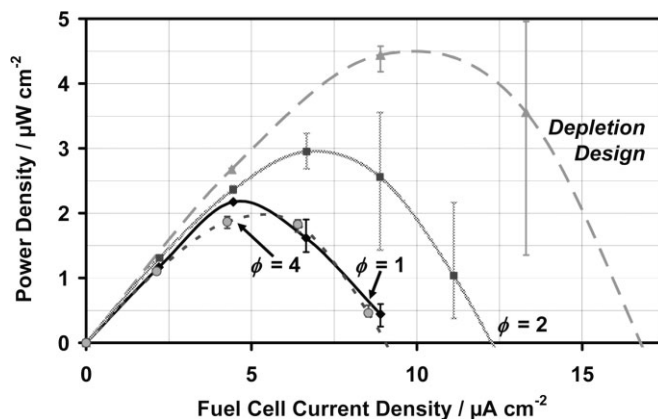
Fig. 8 Comparison of power densities (normalised to base area of the fuel cell) for a *single layer fuel cell* assembled with equally sized electrodes (solid black line), with a cathode to anode area proportion of 2:1 (solid line) and 4:1 (dashed line). A fuel cell assembled in *depletion design* presented in a dashed grey line. Bars represent min- and max-values out of three experiments.

No performance enhancement is obtained with a cathode area proportion of $\phi = 4$. Here, the maximum power density amounts to only 1.9 $\pm$ 0.1 μW cm^{-2} observed at a fuel cell current density of 4.3 μA cm^{-2}. As can be seen from Figure 7 this stems from an MTL at the anode, which faces four times the local electrode current density as in the case of equally sized electrodes ($\phi = 1$).

3.3.2 Derivation of Maximum Power Densities in Dependence of the Cathode Area Proportion ϕ

The previous experiments showed that the optimum cathode area proportion has to be chosen as a compromise of MTL effects occurring at the two fuel cell electrodes. To estimate this optimum cathode area proportion ϕ_{max} and therefore the maximum capability of *single layer fuel cells* in terms of power density we in the following utilise an analytical model to calculate maximum power densities as a function of the applied cathode area proportion (see appendix for details).

The here performed calculation is based on the following assumptions: first, the occurrence of the maximum power density is reached within the linear current density range of cathode and anode. Second, activation losses in the polarisation curve are neglected. Both simplifications are supported by the previously shown experimental results.

In this model the experimentally observed average values of open circuit voltage (OCV = OCP$_{Cath}$ $-$ OCP$_{An}$), area specific resistances R_{Pol} and limits of the linear current density range (see Table 3) were utilised to calculate polarisation curves in dependence of the cathode to anode area proportion ϕ:

$$P(j_{FC}, \Phi) = j_{FC}\left[\text{OCV} - j_{FC}(\Phi + 1)\left(\frac{|R_{Pol,Cath}|}{\Phi} + |R_{Pol,An}|\right)\right] \quad (7)$$

To account for MTL the local cathode and anode current densities were limited to their experimentally evaluated lin-
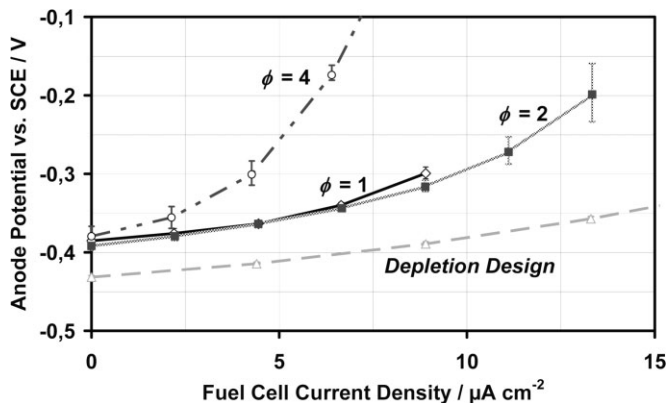

Fig. 7 Anode polarisation curves in *single layer fuel cells* normalised to the fuel cell base area. Anodes operated in *depletion design* are shown for comparison. Bars represent min- and max-values out of three experiments.

Fuel Cells

Table 3 Average values of OCV, area specific resistances (R_{Pol}), and Ohmic limits (j_{lim}) observed from all previously shown *single layer fuel cell* experiments. Area specific resistances are normalised to their local electrode area. Ohmic limits were estimated from the experimental data by taking the maximum local current density for which a linear curve progression was observed during recording of the polarisation curves. Due to the limited number of data points this is an underestimation of the exact value.

			Anode	Cathode
Area specific resistance	R_{Pol}	($k\Omega$ cm^{-2})	3.7 ± 1.0	-11.8 ± 3.9
Ohmic limit	j_{lim}	(μA cm^{-2})	26.7[a]	10.7[b]
Open circuit voltage	OCV	(mV)	602 ± 40	

[a] Observed for $\phi = 2$.
[b] Observed for $\phi = 4$.

ear ranges (up to $j_{Cath,lim}$, $j_{An,lim}$ as listed in Table 3). As a consequence of the two different MTL phenomena, the resulting equation for the calculation of the maximum power density contains two branches:

$$P_{max}(\Phi) = $$

$$\begin{cases} \dfrac{\Phi j_{Cath,lim}}{\Phi+1}\left(OCV - \Phi j_{Cath,lim}\left(\dfrac{|R_{Pol,Cath}|}{\Phi} + |R_{Pol,An}|\right)\right) & \text{if} \quad \Phi < \dfrac{j_{An,lim}}{j_{Cath,lim}} \\[3mm] \dfrac{j_{An,lim}}{\Phi+1}\left(OCV - j_{An,lim}\left(\dfrac{|R_{Pol,Cath}|}{\Phi} + |R_{Pol,An}|\right)\right) & \text{if} \quad \Phi > \dfrac{j_{An,lim}}{j_{Cath,lim}} \end{cases}$$

$$(8)$$

Figure 9 presents the accordingly calculated maximum power densities as a function of the cathode area proportion. A maximum power density of 2.9 μW cm^{-2} is found for an optimum cathode area proportion of $\phi_{max} = 2.4$. At this cathode area proportion the boundary conditions set due to MTL at cathode and anode equally limit the achievable power density. For $\phi < \phi_{max}$ the system is predominantly limited by MTL at the cathode whereas for $\phi > \phi_{max}$ MTL at the anode is the dominating effect. This characteristic behaviour corresponds to the experimental observations.

The grey area in Figure 9 represents the uncertainty in the calculated maximum power density according to the experi-
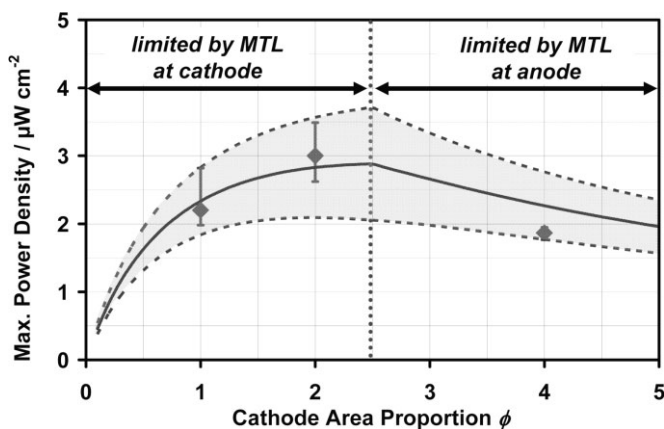

Fig. 9 Derived maximum power densities of *single layer fuel cells* as a function of their cathode area proportions under consideration of MTL. The grey area represents the variation of the calculated maximum power densities as consequence of the standard deviations of the input parameters: OCV, $R_{Pol,Cath}$ and $R_{Pol,An}$ given in Table 3.

mentally observed batch to batch variation expressed by the standard deviations in polarisation resistance of the individual electrodes as well as in OCV, listed in Table 3.

From the calculation a power density of 2.8 μW cm^{-2} is predicted for a cathode area proportion of $\phi = 2$, based on an average electrode performance according to Table 3. This is in agreement with the experimentally observed maximum power density of 3.0 $\pm$ 0.3 μW cm^{-2}. For the cathode area proportion of $\phi = 1$ and 4 the maximum power density is overestimated by the calculation, but the values are still within the uncertainty range represented by the grey area. This is mostly because for these cathode area proportions the OCV values obtained in the experiment (575 ± 20 mV for $\phi = 1$ and 578 ± 4 mV for $\phi = 4$) are below the average OCV value of 602 ± 41 mV used in the calculation.

4 Conclusion

In the present work we took advantage of the high oxygen tolerance of Raney-platinum film anodes to demonstrate the feasibility of an implantable glucose fuel cell assembled in *single layer design*. With equally sized electrodes we obtained a power density of 2.2 $\pm$ 0.1 μW cm^{-2}. This corresponds to 50% of the power density achieved in *depletion design*, reflecting the two times higher available electrode area in *depletion design* due to stacking of the electrode. Moreover, this shows that oxygen depletion has no significant effect on power output in case of using the oxygen-tolerant Raney-platinum film electrodes. Despite a lower power density, placing cathode and anode side by side according to the novel *single layer fuel cell design* has several advantages for application: first, its simplicity – it requires no permeable cathode structure, no layer stacking and no lateral framework. Second, its thickness – implemented as a single layer this fuel cell design can easily be realised as a thin-layer coating on the surface of implant capsules. Third, *single layer fuel cells* offer the opportunity to adjust the cathode to anode area proportion and hence to find an optimum balance between anodic and cathodic MTL. Such an optimum balance can be estimated by the analytical model introduced in this work, which was found to be in accordance with experimental results. Calculated from the linear polarisation resistance of the individual electrodes used in this work the optimum cathode to anode area proportion of 2.4 yields a maximum power density of 2.9 μW cm^{-2}. Hence, optimised *single layer fuel cells* exhibit a power density which is only by only 34% lower compared to conventional *depletion design*. Furthermore, enlarged cathode area proportions represent an opportunity for cost reduction since the 500 nm thin cathode layer requires significantly less platinum than the 50 μm thick anode.

Based on the present work the implementation of the fuel cell would still mandate the mounting of separately fabricated self-supporting electrode structures onto an implant capsule. In future this could be facilitated by the application of electrochemical or hydrothermal techniques that allow for

the direct deposition of highly porous platinum catalysts onto the electrically conducting implant surface [34, 35]. Besides fabrication and assembly design issues as discussed in this have to be focused in particular on the long-term stability of the electrode catalysts. In their present form they still show strong performance degradation in physiological environment [25, 27]. Therefore, surface modifications of the electrocatalyst with additional elements to form bi-or tri- metallic catalysts are under current investigation. In other fuel cell systems, this strategy enabled a significantly faster product desorption and lower sensitivity towards interfering substances [36–39].

Acknowledgements

Appendix

Derivation of Maximum Power Densities as a Function of the Cathode Area Proportion

Calculation of Polarisation Curves

The here presented model is a tool to calculate polarisation curves in dependence of the cathode area proportion ϕ. Polarisation curves are derived on the basis of experimentally determined electrode properties (OCV, area specific resistance) and the following two assumptions, both of which were confirmed by the experimental results:

(i) The maximum in power density is observed within the linear current density range of the polarisation curve.

(ii) Activation losses in polarisation curve progression are negligible.

Hence, the linear range of a polarisation curve can be calculated for *single layer fuel cells* from the OCV and Ohmic losses:

$$U(j_{FC}) = \text{OCV} - j_{FC}\, R_{Pol,FC}(\Phi) \tag{A1}$$

Here, the Ohmic losses are derived from the applied fuel cell current density j_{FC} and the area specific resistance of the fuel cell $R_{Pol,FC}(\phi)$. This area specific resistance $R_{Pol,FC}$ of the fuel cell can be expressed by the separate area specific resistances of cathode ($R_{Pol,Cath}$) and anode ($R_{Pol,An}$) listed in Table 3 in combination with a conversion factor for the local electrode current densities:

$$R_{Pol,FC}(\Phi) = \frac{\Phi+1}{\Phi}\left|R_{Pol,Cath}\right| + (\Phi+1)\left|R_{Pol,An}\right| \tag{A2}$$

Derivation of the Fuel Cell Current Density at Maximum Power Density $j_{FC,max}(\phi)$

In a next step the fuel cell current density $j_{FC,max}(\phi)$ at which the maximum power density is reached is calculated by solving:

$$0 = \frac{\partial P(j_{FC}, \Phi)}{\partial j_{FC}} = \frac{\partial}{\partial j_{FC}}[j_{FC}\, U(j_{FC}, \Phi)] \tag{A3}$$

$$j_{FC,max}(\Phi) = \frac{\Phi\,\text{OCV}}{2\,(1+\Phi)\,\left(\left|R_{Pol,Cath}\right| + \Phi\left|R_{Pol,An}\right|\right)} \tag{A4}$$

To account for the MTL the fuel cell current density has to be limited according to the upper limits of the linear current density ranges observed for cathode ($10.7\ \mu\text{A cm}^{-2}$) and anode ($26.7\ \mu\text{A cm}^{-2}$) according to Eq. (A5)

$$j_{FC,max}(\Phi) = \text{Min}\left\{\begin{array}{c} \frac{\Phi\,\text{OCV}}{2\,(1+\Phi)\,\left(\left|R_{Pol,Cath}\right| + \Phi\left|R_{Pol,An}\right|\right)} \\ j_{Cath,lim}\,\frac{\Phi}{\Phi+1} \\ j_{An,lim}\,\frac{1}{\Phi+1} \end{array}\right\} \tag{A5}$$

Here, $j_{Cath,lim}$ and $j_{An,lim}$ stand for the experimentally determined upper limits of the linear local current density ranges of cathode and anode, respectively. The here derived function for $j_{FC,max}(\phi)$ is plotted in Figure A1, showing that its minimum is always defined by an MTL predominantly occurring either at the cathode or at the anode depending on ϕ. MTL at the cathode is the dominant effect determining the upper limit of the linear fuel cell polarisation range if

$$\Phi < \frac{j_{An,lim}}{j_{Cath,lim}} \tag{A6}$$

Otherwise MTLs occurring at the anode define the upper limit of the linear fuel cell current density range.
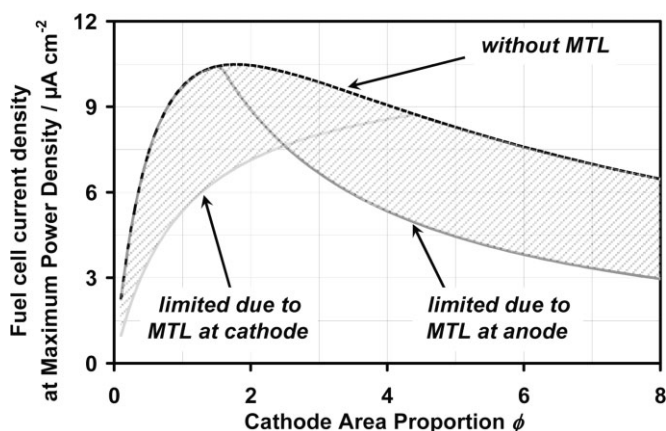

Fig. A1 Graphical illustration of the evolution of the criterion derived as Eq. (A6). The minimum of the presented lines corresponds to the maximum achievable fuel cell current densities without the occurrence of MTL. The red area represents the losses caused by MTLs compared to the ideal (non-limited mass transport).

Fuel Cells

Derivation of Maximum Power Densities $P_{max}(\phi)$

Finally, fuel cell power densities can be calculated according to:

$$P_{\max}(\Phi) = j_{Fc,\lim}(\Phi)\, U\big(j_{Fc,lim}(\Phi),\Phi\big) \tag{A7}$$

Under consideration of the previously derived criterion [Eq. (A6)] a function for the calculation of maximum power densities results that is divided into two branches:

$$P_{\max}(\Phi) =
\begin{cases}
\dfrac{\Phi\, j_{Cath,\lim}}{\Phi+1}\left(OCV - \Phi\, j_{Cath,\lim}\left(\dfrac{|R_{Pol,Cath}|}{\Phi} + |R_{Pol,An}|\right)\right) & \text{if} \quad \Phi < \dfrac{j_{An,\lim}}{j_{Cath,\lim}} \\[4mm]
\dfrac{j_{An,\lim}}{\Phi+1}\left(OCV - j_{An,\lim}\left(\dfrac{|R_{Pol,Cath}|}{\Phi} + |R_{Pol,An}|\right)\right) & \text{if} \quad \Phi > \dfrac{j_{An,\lim}}{j_{Cath,\lim}}
\end{cases}
\tag{A8}$$

List of Symbols

Latin Letters

A	Geometric area (cm^2)
j	Current density ($\mu A\ cm^{-2}$)
OCP	Open circuit potential (V *vs.* SCE)
OCV	Open circuit voltage (V)
P	Power density ($\mu W\ cm^{-2}$)
PBS	Phosphate buffered saline
R_{Pol}	Area specific resistance ($k\Omega\ cm^{-2}$)
RF	Roughness factor
SCE	Standard calomel electrode
U	Voltage (V)

Greek letters

ϕ	Cathode to anode area proportion

Subscripts

An	Anode
Cath	Cathode
FC	Fuel cell
lim	Limit of the linear Ohmic current density range
max	Maximum

References

[1] S. Kerzenmacher, J. Ducrée, R. Zengerle, F. von Stetten, *J. Power Sources* **2008**, *182*, 1.

[2] R. A. M. Receveur, F. W. Lindemans, N. F. de Rooij, *J. Micromech. Microeng.* **2007**, *17*, R50.

[3] J. R. Rao, G. Richter, *Naturwissenschaften* **1974**, *61*, 200.

[4] J. R. Rao, G. J. Richter, F. von Sturm, E. Weidlich, *Bioelectrochem. Bioeng.* **1976**, *3*, 139.

[5] J. R. Rao, G. J. Richter, F. von Sturm, E. Weidlich, *Bioelectrochem. Bioeng.* **1977**, *4*, 104.

[6] R. A. Bullen, T. C. Arnot, J. B. Lakeman, F. C. Walsh, *Biosens. Bioelectron.* **2006**, *21*, 2015.

[7] E. Katz, I. Willner, *J. Am. Chem. Soc.* **2003**, *125*, 6803.

[8] N. Mano, F. Mao, A. Heller, *J. Am. Chem. Soc.* **2003**, *125*, 6588.

[9] S. C. Barton, J. Gallaway, P. Atanassov, *Chem. Rev.* **2004**, *104*, 4867.

[10] A. Heller, B. Feldman, *Chem. Rev.* **2008**, *108*, 2482.

[11] P. Cinquin, C. Gondran, F. Giroud, S. Mazabrard, A. Pellissier, F. Boucher, J. P. Alcaraz, K. Gorgy, F. Lenouvel, S. Mathé, P. Porcu, S. Cosnier, *PLoS One* **2010**, *5*, e10476.

[12] A. Heller, *Anal. Bioanal. Chem.* **2006**, *385*, 469.

[13] A. Ramanavicius, A. Ramanaviciene, *Fuel Cells* **2009**, *9*, 25.

[14] C. P. B. Siu, M. Chiao, *J. Microelectromech. S.* **2008**, *17*, 1329.

[15] Y. Han, C. Yu, H. Liu, *Biosens. Bioelectron.* **2010**, *25*, 2156.

[16] A. Habrioux, E. Sibert, K. Servat, W. Vogel, K. B. Kokoh, N. Alonso-Vante, *J. Phys. Chem. B* **2007**, *111*, 10329.

[17] Y. K. Choi, G. Wang, M. H. Nayfeh, S. T. Yau, *Biosens. Bioelectron.* **2009**, *24*, 3103.

[18] R. F. Drake, B. K. Kusserow, S. Messinger, S. Matsuda, *Trans. Am. Soc. Artif. Int. Organs* **1970**, *16*, 199.

[19] L. S. Y. Wong, S. Hossain, A. Ta, J. Edvinsson, D. H. Rivas, H. Naas, *IEEE J. Solid-State Circuits* **2004**, *39*, 2446.

[20] J. R. Rao, G. Richter, F. von Sturm, E. Weidlich, *Ber. Bunsen Phys. Chem.* **1973**, *77*, 787.

[21] D. A. Gough, F. L. Anderson, J. Giner, C. K. Colton, J. S. Soeldner, *Anal. Chem.* **1978**, *50*, 941.

[22] D. G. Maggs, R. Jacob, F. Rife, R. Lange, P. Leone, M. J. During, W. V. Tamborlane, R. S. Sherwin, *J. Clin. Invest.* **1995**, *96*, 370.

[23] J. R. Rao, G. Richter, E. Weidlich, F. von Sturm, *Phys. Med. Biol.* **1972**, *17*, 738.

[24] S. Kerzenmacher, U. Kräling, T. Metz, J. Ducrée, R. Zengerle, F. von Stetten, *J. Power Sources* **2010**, *196*, 1264.

[25] S. Kerzenmacher, M. Schroeder, R. Brämer, R. Zengerle, F. von Stetten, *J. Power Sources* **2010**, *195*, 6516.

[26] S. Trasatti, O. A. Petrii, *J. Electroanal. Chem.* **1992**, *327*, 353.

[27] S. Kerzenmacher, U. Kräling, M. Schroeder, R. Brämer, R. Zengerle, F. von Stetten, *J. Power Sources* **2010**, *195*, 6524.

[28] P. D. van der Wal, M. Dadras, M. Koudelka-Hep, N. F. de Rooij, "Modification ot the surface roughness of platinum thin film electrodes by alloy formation with aluminum", presented at *206th Meeting of Electrochemical Society*, Honolulu, Hawaii, 10 August, 2004.

[29] S. Kerzenmacher, K. Mutschler, U. Kräling, H. Baumer, J. Ducrée, R. Zengerle, F. von Stetten, *J. Appl. Electrochem.* **2009**, *39*, 1477.

[30] S. Kerzenmacher, J. Ducrée, R. Zengerle, F. von Stetten, *J. Power Sources* **2008**, *182*, 66.

[31] A. A. Sharkawy, B. Klitzman, G. A. Truskey, W. M. Reichert, *J. Biomed. Mater. Res.* **1997**, *37*, 401.

[32] J. H. Yuan, K. Wang, X. H. Xia, *Adv. Funct. Mater.* **2005**, *15*, 803.

[33] Y. Y. Song, D. Zhang, W. Gao, X. H. Xia, *Chem.-A Eur. J.* **2005**, *11*, 2177.

[34] A. Kloke, S. Kerzenmacher, R. Zengerle, F. von Stetten, "Facile Fabrication of Ultra Porous Platinum Electrodes and Their Application for Energy Harvesting Glucose Fuel Cells", presented at *ECS 215th Meeting*, San Francisco, CA, **2009**.

[35] K. Koczkur, Q. F. Yi, A. C. Chen, *Adv. Mater.* **2007**, *19*, 2648.

[36] J. Shim, D. Y. Yoo, J. S. Lee, *Electrochim. Acta* **2000**, *45*, 1943.

[37] S. Uhm, H. Jin Lee, Y. Kwon, J. Lee, *Angew. Chem., Int. Ed.* **2008**, *47*, 10163.

[38] S. Kang, J. Lee, J. K. Lee, S. Y. Chung, Y. Tak, *J. Phys. Chem. B* **2006**, *110*, 7270.

[39] J. H. Choi, K. J. Jeong, Y. Dong, J. Han, T. H. Lim, J. S. Lee, Y. E. Sung, *J. Power Sources* **2006**, *163*, 71.